Direct noise predictions of fan broadband noise using LES and analytical models

Jean Al-Am, Vincent Clair, Alexis Giauque, Jérôme Boudet, Fernando Gea-Aguilera

Direct noise predictions of fan broadband noise using LES and analytical models

J. Al Am* and V. Clair, A. Giauque, J. Boudet,
Univ Lyon, École Centrale de Lyon, INSA Lyon, Université Claude Bernard Lyon I, CNRS, Laboratoire de Mécanique des Fluides et d'Acoustique, UMR 5509, 36 Avenue Guy de Collongue, F-69134, Ecully, France

F. Gea-Aguilera †
Safran Aircraft Engines, 77550 Moissy-Cramayel, France

In the present study, we analyze the broadband noise of an ultra high by-pass ratio fan/OGV stage developed at Ecole Centrale de Lyon. Wall-modeled large eddy simulations (LES) of a periodic fan/OGV sector are performed at approach conditions on an unstructured grid that is well refined for direct noise propagation. Comparisons between wall-resolved and wall-modeled computations are performed using a 2.5D simplified configuration of the fan/OGV stage, and show a good agreement. This justifies the use of wall-modeled simulations for the full-span configuration. A good agreement is found between LES and RANS aerodynamic results. However, some differences can be found in the tip gap region and near the hub, where large coherent structures appear. Additionally, a small recirculation bubble can be observed from approximately 60% of the fan blade span in the LES. In this study, the broadband noise is directly computed from the fully-compressible LES solver and compared with predictions from available analytical models. The input data for the analytical models, such as mean and turbulent flow statistics, are obtained from the LES computation. A good agreement is found for the predicted sound power levels between direct LES noise predictions and the LES-informed analytical models. This confirms the capability of the LES numerical setup to directly predict far-field noise. However, some discrepancies can be observed at low frequencies. These might be attributed to the additional noise sources that are present in the LES, which are not considered by the analytical models.

Nomenclature

LES	=	large eddy simulations
RANS	=	Reynolds-averaged Naviers-Stokes
OGV	=	outlet guide vanes
UHBR	=	ultra high by-pass ratio
NSCBC	=	Navier-Stokes characteristic boundary conditions
TE	=	trailing edge
LE	=	leading edge
WM	=	wall-modeled
WR	=	wall-resolved
PSD	=	power spectral density
RSI	=	rotor-stator interaction
BPF	=	blade passing frequency
VPF	=	vane passing frequency
TLV	=	tip leakage vortex
SWL	=	sound power level
RMS	=	root mean square
c	=	chord [m]
Δt	=	time step [s]

*PhD candidate, Ecole Centrale de Lyon, LMFA, jean.al-am@ec-lyon.fr.
†R&D Acoustics Engineer, Aerodynamics and Acoustics Department, fernando.gea-aguilera@safrangroup.com.

M_{is}	=	isentropic Mach number
C_f	=	friction coefficient
x, y, z	=	streamwise, transverse and spanwise Cartesian coordinates, respectively [m]
θ	=	azimuthal direction
r	=	radial direction
$\dot{m}$	=	mass flow rate [kg/s]
δ_1	=	boundary layer displacement thickness [m]
δ_2	=	boundary layer momentum thickness [m]
H_{12}	=	boundary layer shape factor
ρ	=	density [kg/m^3]
p	=	static pressure [Pa]
p'	=	pressure fluctuations [Pa]
p_{rms}	=	rms pressure fluctuations [Pa]
u_{rms}	=	rms streamwise velocity fluctuations [m/s]
P_0	=	total pressure [Pa]
T_0	=	total temperature [K]
c_0	=	speed of sound [m/s]
f	=	frequency [Hz]
f_c	=	cut-off frequency [Hz]
ω	=	angular frequency [rad/s]
R_S	=	shroud radius [m]
R_H	=	hub radius [m]
H	=	span height [m]
Ω	=	rotational speed [rpm]
u	=	streamwise velocity component [m/s]
u_b	=	streamwise velocity component in the boundary layer [m/s]
$\nabla \dot{u}$	=	dilatation rate [1/s]
u^+	=	dimensionless wall velocity
x^+, y^+, z^+	=	dimensionless wall distances in the streamwise, transverse and spanwise directions, respectively
V_x, V_θ, V_{rad}	=	Axial, circumferential and radial components of the velocity, respectively [m/s]
T_u	=	turbulence intensity
λ	=	turbulence integral length scale [m]
λ_{Ta}	=	Taylor micro-scale [m]
M	=	Mach number
λ_{ac}	=	acoustic wavelength [m]
ν	=	kinematic viscosity [m^2/s]
k_t	=	turbulent kinetic energy [m^2/s^2]
ϵ	=	turbulent dissipation rate [m^2/s^3]
ω_t	=	specific rate of dissipation of the turbulent kinetic energy [m^2/s^3]
γ_h	=	specific heats ratio
U	=	free-stream velocity magnitude [m/s]
γ	=	two-point coherence function
l_z	=	spanwise correlation length [m]
Δz	=	spanwise distance [m]
k_z	=	spanwise wavenumber [m^{-1}]
Φ_{pp}	=	power spectral density of wall-pressure fluctuations [Pa^2/Hz]
Φ_{uu}	=	power spectral density of streamwise velocity fluctuations [m^2/s]

I. Introduction

Today, the reduction of noise from aircraft engines close to airports, particularly during the take-off and approach conditions, is one of the main objectives of engine manufacturers. Modern aero-engines, such as ultra high by-pass ratio (UHBR) turbofan engines, present a reduced rotational speed, an increased by-pass ratio and a large fan diameter. These features aim at improving the engine efficiency, and will be useful to meet future regulations and guidelines for

sustainable aviation, such as those from the ACARE flight path 2050 [1]. For UHBR turbofan engines, the fan-outlet guide vane (OGV) stage becomes one of the main contributors to the noise emissions [2, 3]. The tonal noise from the fan-OGV stage has already been addressed in the literature and many solutions have been proposed to reduce tonal noise. For example, acoustic liners at the inlet and exhaust duct of the nacelle can be implemented to damp propagating tones [4]. The blade count can also be optimized to take advantage of duct filtering [5] and to cut off the blade passing frequency (BPF). At approach condition, the broadband noise from the fan/OGV stage is a major contributor to the overall noise level [6, 7]. Broadband noise is less documented in the literature than tonal noise due to its stochastic nature, which is associated with the turbulence in the boundary layers and the wakes. Furthermore, broadband noise is difficult to attenuate due to the large range of cut-on modes that contribute to each frequency in the noise spectrum [7]. Several mechanisms can produce broadband noise, such as the interaction of the inlet turbulence with the rotor blades, vortex noise in the tip region of the rotor, trailing edge noise and rotor-stator interaction noise. Trailing edge noise is generated by the turbulence in boundary layers passing the trailing edge of the blades or the vanes. Rotor-stator interaction noise results from the interaction of turbulence in the rotor wakes with the leading edge of the stator, which generates an unsteady loading on the vanes. The rotor-stator interaction noise mechanism is often considered to be the dominant noise source of the fan stage at approach condition [7, 8]. Over the past few decades, several techniques have been developed to model and predict both trailing edge and rotor-stator interaction noise [3, 9].

Recent progress in computing resources has allowed for a detailed description of the turbulent flow in turbomachinery applications using high-fidelity simulations, such as large eddy simulation (LES) and direct numerical simulation (DNS). These numerical simulations can describe the turbulent structures in the flow that produce broadband noise. The DNS is still limited to applications at low Reynolds numbers and to academic configurations due to its expensive computational cost. LES is preferred for the current study to model complex flows in a fan stage with sufficient accuracy at an acceptable computational cost. Using LES, several methodologies can be used to predict noise sources and acoustic propagation to the far-field. The present study focuses on two different methodologies, (i) LES-informed analytical models, and (ii) LES direct noise computations.

Several analytical models are available for the prediction of fan broadband noise [8, 9]. Initial analytical models considered either the turbulent flow impinging on the leading edge of an isolated airfoil or the diffraction of a turbulent boundary layer at the airfoil TE [10–12]. The use of such models to predict fan broadband noise requires the assumption of an isolated blade or vane. This may be appropriate for low solidity rotors and stators, such as in open-rotor engines. However, cascade effects due to the high solidity of blades and vanes in a ducted fan stage have to be accounted for.

The rotor-stator interaction noise models used in this study, which account for the cascade effects were developped by Hanson [13] and Posson *et al.* [14, 15]. These models are based on the previous work of Glegg [16] and have been developed to predict the rotor-stator interaction noise from cascade configurations and non-uniform flows in the spanwise direction through the use of the strip theory. In Hanson's model, the acoustic waves from each strip of the vanes are propagated into the free-field by assuming a uniform mean flow. In Posson's model, the unsteady loading from the vanes is used as a dipole source term in an in-duct acoustic analogy [15, 17, 18]. Thus, duct wall effects are accounted for when using Posson's model, whereas these are neglected in Hanson's model. The trailing edge noise model adopted in this study is based on Amiet's work, which describes the scattering of pressure fluctuations from a turbulent boundary layer at the trailing edge [12, 19]. An in-duct acoustic analogy is used for the noise propagation. For comparison purposes, LES mean and turbulent flow parameters from the rotor wakes and the boundary layers are used as inputs for these analytical models in the present study.

Noise predictions from analytical models are compared to direct noise computations from LES. These do not rely on assumptions that are made in analytical models, such as flat plate airfoils, uniform mean flows and isotropic turbulence. The direct noise computation from the LES requires a specific mesh refinement and numerical setup, which increases the computational cost when compared to analytical models or hybrid methods using an acoustic analogy for the noise propagation. However, an increased accuracy in noise predictions can be expected from direct noise predictions.

The main objective of this work is to compare direct noise predictions of a fan/OGV stage using LES with the noise predictions from LES-informed analytical models to improve current understanding of fan broadband noise. The paper is organized as follows. Section II presents the fan stage configuration, the numerical setup and the mesh characteristics. Section III includes a mesh convergence analysis. The flow topology and the aerodynamic results are presented in Section IV. Finally, noise predictions from the two methodologies, i.e. the direct LES noise computation and the LES-informed analytical models, are discussed in Section V.

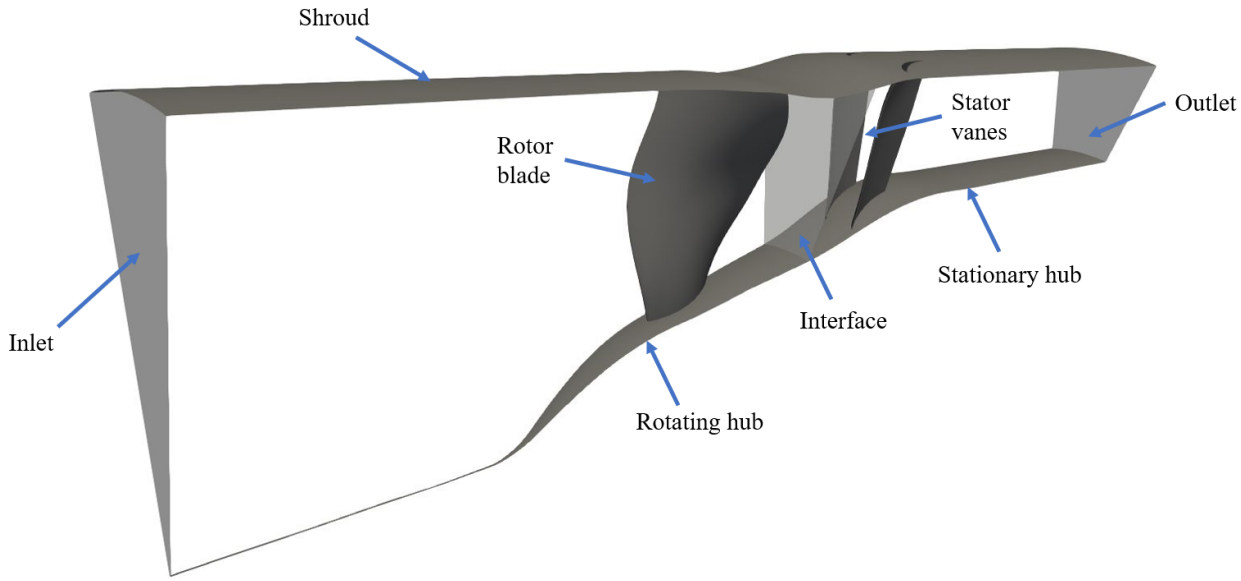

Fig. 1 Computational domain of the ECL5 fan/OGV stage for both LES and RANS simulations.

II. Numerical setup

A. ECL5 fan stage configuration

In the present work, LES are performed on the ECL5 fan/OGV stage, which is a new open test case designed at Ecole Centrale de Lyon [20, 21]. The ECL5 fan/OGV stage is based on an UHBR aero-engine with a low rotational speed and without core flow, which has been designed using technical requirements for a mid-range commercial aircraft. The ECL5 fan/OGV stage is composed of 16 rotor blades and 31 stator vanes. It should be noted that such a low-count OGV is expected to be cut-on for the BPF, which leads to a significant tonal noise contribution. The main geometric characteristics are detailed here. The hub-to-shroud ratio at the fan leading edge position is 0.29. The hub radius is $R_H = 82$ mm just upstream of the rotor and $R_H = 150$ mm downstream of the stator. The shroud radius is $R_S = 250$ mm upstream of the rotor and $R_S = 252$ mm downstream of the stator. The chord length at mid-span is $c = 101$ mm for the rotor blade and $c = 69$ mm for the stator vane. The minimum rotor-stator distance is 110 mm (slightly greater than the mid-span rotor chord length), which is expected to minimize potential effects. The pressure ratio at the fan blade tip was minimized to reduce the tip clearance flow. The tip clearance at approach condition is set to 0.965 mm ($0.011c$) at the leading edge and 1.27 mm ($0.014c$) at the trailing edge. The ECL5 fan blades are highly twisted, which is related to the small hub-to-shroud ratio. The stagger angle varies from 2° on the hub to -58° on the tip.

B. Computational domain

A periodic fan/OGV sector is simulated to reduce the computational cost of the LES. The AVBP solver [22] that is used for the LES in this work requires the same angular extent for the rotor and stator domains. Thus, the initial 31 OGVs are adapted to 32 OGVs to allow for a $2\pi/16$ angular periodicity and reduce the computational domain. The solidity of the OGV, which is defined as the ratio between the chord length and the inter-vane spacing, is maintained by adjusting the chord length to keep the stage performance [23]. The modified chord length of the stator vanes at the mid-span is 66.8 mm. Two different configurations of the periodic sector are considered in the present study: (i) a radial slice sector and (ii) a full-span sector. For the first case, the radial slice is extracted at 80% of the fan span and has a radial extension of about 12% of the full-span. The airfoil shape is kept constant throughout the span of the radial slice. Such a simplified case is only used for mesh convergence purposes. The reduced computational domain allows us to compare wall-resolved (WR) and wall-modeled (WM) LES. All the noise predictions and the comparisons with analytical models are performed for the full-span case. The same wall model and numerical setup are used for both the radial slice and the full-span cases. An overview of the computational domain (for the full-span case) is shown in Figure 1. The domain extends from 3.75 fan chord lengths upstream of the fan leading edge to 4.25 vane chord lengths

downstream of the OGVs. The distance upstream of the rotor is chosen to ensure a well-developed boundary layer on the casing.

The present simulations are performed at approach conditions (Ω = 6050 rpm, which corresponds to 55% of the nominal rotational speed). For this operating point, the axial Mach number is set to 0.29 at the inflow and the relative Mach number at the fan blade tip is approximately 0.6. The circumferential Mach number at the blade tip corresponds to 0.48 and the BPF is equal to 1613 Hz.

C. LES numerical parameters

In the present study, the LES governing equations are solved using the AVBP solver, which is an explicit unstructured fully compressible LES solver developed by CERFACS [22]. For turbomachinery applications, two LES domains are coupled. The first one is the rotor domain that contains the fan blade, and the second one is the stator domain that contains the stator vanes. The coupler CWIPI is used for the data exchange between the two domains, which is based on an overlapping grid method [24].

A third order, finite-volume, two steps Taylor Galerkin (TTGC) [25] convective scheme is used to solve the filtered Navier-Stokes equations. The SIGMA sub-grid scale model [26] is used to account for the unresolved turbulent eddies. Non-reflecting Navier-Stokes characteristic boundary conditions (NSCBC) [27] are used at the inlet and the outlet sections. At the inlet section, a uniform mean flow is injected in the axial direction, the total pressure is set to P_0=101325 Pa and the total temperature is set to T_0=300 K. At the outlet section, the pressure is adjusted to obtain the desired mass flow rate. On the azimuthal boundaries of the computational domain, periodic boundary conditions are used. On the wall surfaces, including the blade, vanes, shroud and hub, a no-slip boundary condition is used. The inner part of the boundary layer is modeled using a wall law [28], with a dimensionless velocity relative to the wall $u^+ = \frac{1}{\kappa}\ln(Ay^+)$ for $y^+ > 11.45$, with $\kappa = 0.41$ and $A = 9.2$. Below $y^+ = 11.45$, a linear law is imposed. For the radial slice case, a slip wall boundary condition is used at the boundaries in the radial direction. The time step for the simulation is $\Delta t = 2.8 \times 10^{-8}$ s and the computational time is approximately $105 * 10^3$ CPUh per rotation. About three full fan rotations are performed for the numerical and statistical convergence, and four additional fan rotations are performed for the acoustic data collection and post-processing.

D. Mesh characteristics

The mesh at mid-span and in the rotor tip gap is shown in Figure 2. The grid is an unstructured hybrid mesh composed of prismatic cells on the blade walls, tetrahedral cells away from the blades, and pyramidal cells in the transition region between prismatic and tetrahedral cells. The mesh is designed based on both turbulent and acoustic criteria established by the authors in a previous work [29]. This ensures a suitable resolution of the boundary layer and wake turbulence and propagate the acoustic waves over a certain distance without significant dissipation and dispersion errors.

The main mesh properties for the WM-LES and WR-LES cases are given in Table 1. For the near wall refinement, the first layer close to the wall has the smallest spacing, and the cell size is progressively increased using a given expansion ratio. The dimensionless cell sizes, which are given by x^+, y^+ and z^+ in the streamwise, transverse and spanwise directions respectively, are fixed below certain values. Figures 3 and 4 show the y^+ and $x^+ = z^+$ values on the blade and vane surfaces for the full-span WM-LES.

Away from the walls, the mesh is refined based on the following criteria [29]:

- Acoustic criterion. At least 13 points per wavelength ($\lambda_{ac} = \frac{c_0(1-M)}{f_c}$, where c_0 is the speed of sound, M is a mean Mach number, and f_c = 20 kHz is the desired mesh cut-off frequency) are used to ensure a correct propagation of the acoustic waves below a cut-off frequency. This criterion, which depends on the mesh topology and the numerical scheme, is shown to provide accurate results in a previous work [29].
- Turbulent criterion. For an accurate description of the turbulent structures in the wake regions, the mesh size is smaller than 30 times the Taylor micro-scale ($\lambda_{Ta} = (10\frac{\nu k_t}{\epsilon})^{(1/2)}$, where ν is the kinematic viscosity, k_t the turbulent kinetic energy, and ϵ the turbulent dissipation rate).

Using these mesh refinement criteria, different mesh zones can be found in Figure 2 (a). In the tip region, considering prism and tetrahedral cells, 30 points are imposed in the radial direction as shown in Figure 2 (f).

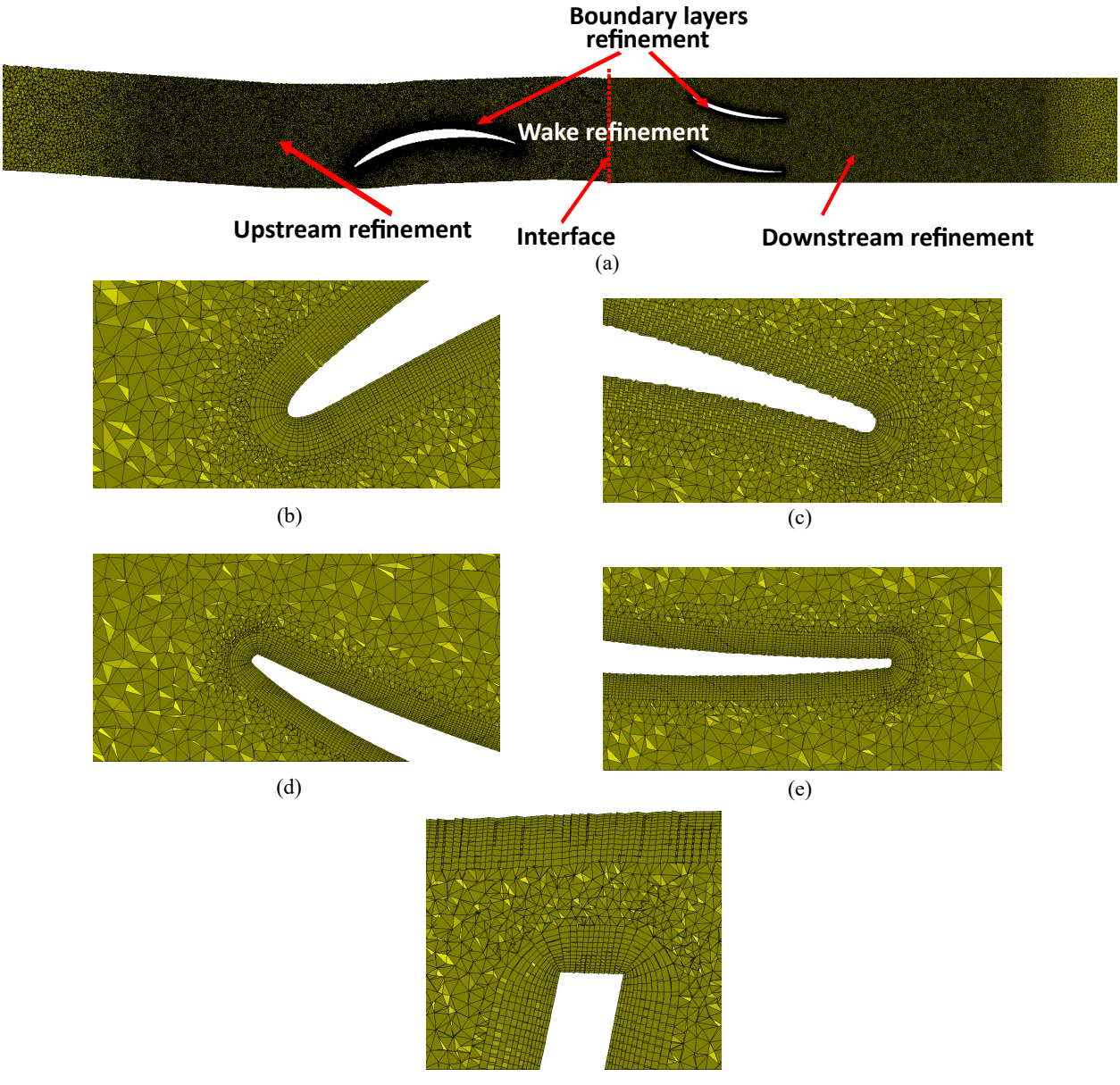

Fig. 2 (a) Grid in a blade-to-blade view at mid-span. Mesh refinements around the rotor leading edge (b), rotor trailing edge (c), stator leading edge (d), stator trailing edge (d) and in the rotor tip gap region (f).

Table 1 Mesh properties for different LES grids. x^+, y^+ and z^+ are the maximum dimensionless wall distances in the streamwise, normal and spanwise directions respectively. "RaSlice" corresponds to the radial slice cases, and "FullSpan" to the full-span case.

	RaSlice-WM	RaSlice-WR	FullSpan-WM
Number of cells [10^6]	40	80	95
x^+/z^+	250	35	150
y^+	30	1.0	25
Number of prism layers	10	16	10
expansion ratio	1.1	1.06	1.1
Time step [10^{-8}s]	2.8	0.8	2.8
CPUh/blade passage [10^3]	50	280	105

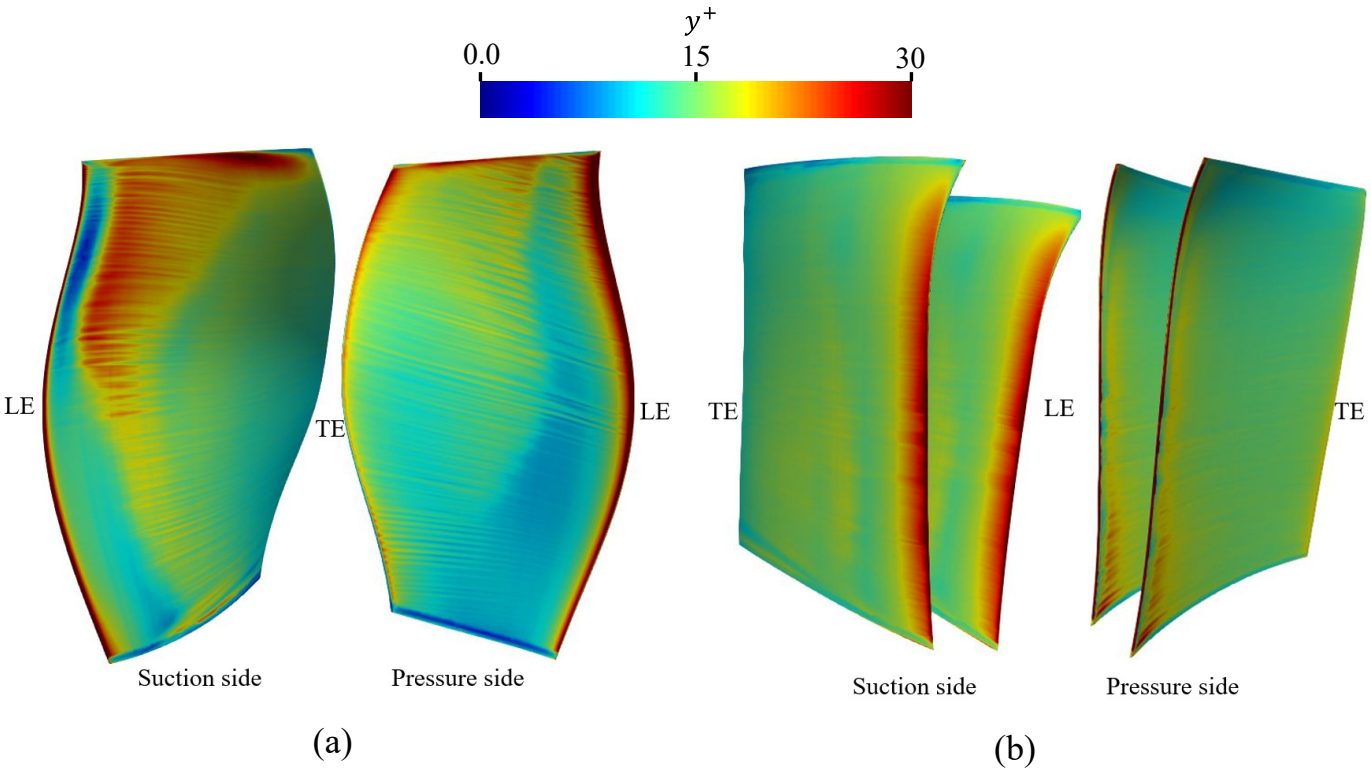

Fig. 3 y^+ values on the rotor blade (a) and stator vanes (b).

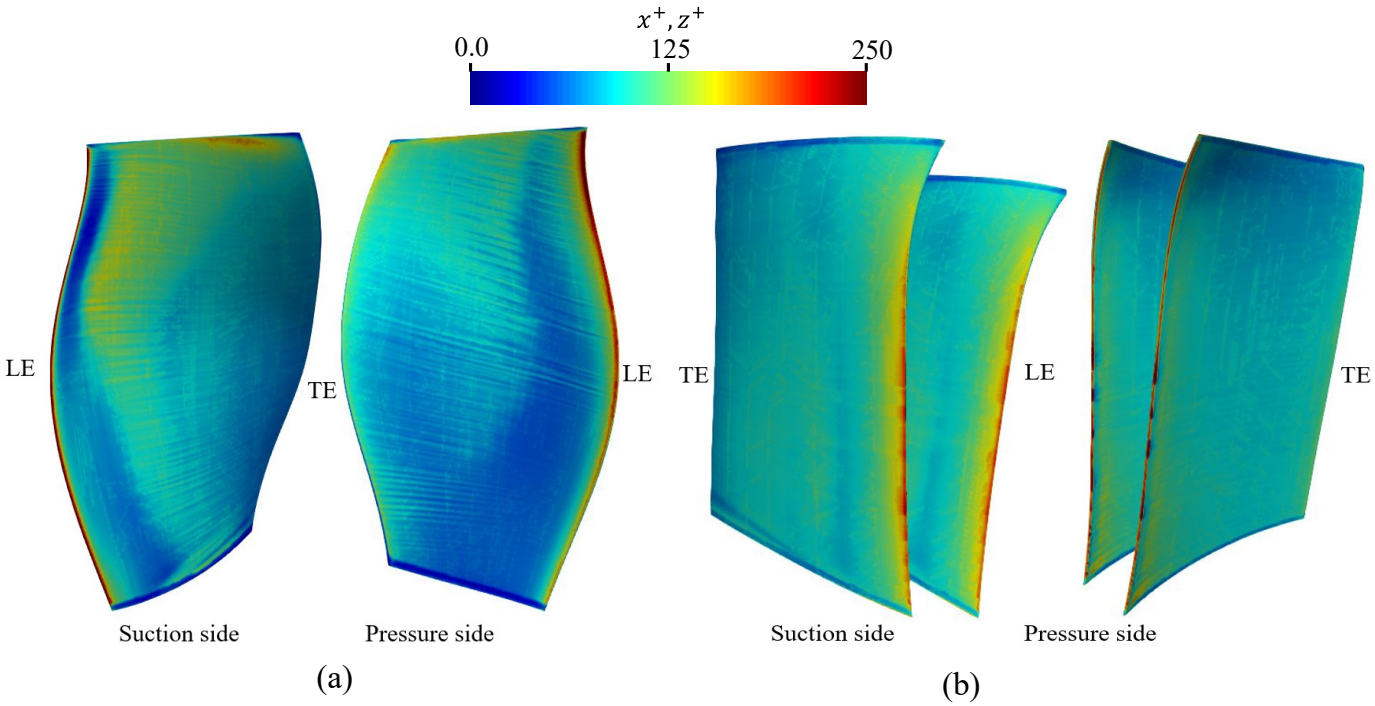

Fig. 4 $x^+ = z^+$ **values on the rotor blade (a) and stator vanes (b).**

E. RANS simulations

RANS simulations are performed for the full-span sector configuration. The OGV geometry is adapted for 32 vanes. This allows us to compare results from LES and RANS simulations. RANS simulations are performed using the *FineTurbo* solver developed by *Numeca International*, using a mixing plane between the fan and the OGVs, and the Jameson-Schmidt-Turkel numerical scheme [30]. Menter's $k-\omega$ SST turbulence model is used [31], which provides improved flow predictions in the presence of adverse pressure gradients in comparison with the Wilcox $k-\omega$ model [32]. Similar input parameters are used for both LES and RANS simulations, i.e, total pressure and temperature are prescribed at the inlet section with a uniform turbulent flow (turbulent intensity of $T_u = 0.5$ % and a turbulence length scale of $\lambda_t = 0.05$ m). On the solid surfaces, a no-slip adiabatic wall boundary condition is adopted. Finally, periodic boundary conditions are imposed on the circumferential boundaries of the computational domain.

A structured multi-block mesh is adopted with 5.1×10^6 grid points, which are distributed on different blocks. The mesh is generated by using *Autogrid V5* developed by *Numeca International*. The mesh uses an O4H block topology, which is a standard block topology for turbomachinery applications and allows for a mesh refinement in certain regions, such as the boundary layers and wakes. The near wall mesh is sufficiently refined to compute the boundary layers without using a wall function. The normalized cell size y^+ varies between 1 and 3 on a large portion of the blade and vanes surfaces with a maximum of 4 at the leading edges. The total cell count in the rotor domain is approximately 3.4 millions, with 131 layers in the radial direction. The fan tip region is discretized using 31 points in the radial direction to correctly capture the complex 3D flow in this region. For the stator domain, 1.8 million cells are used, with 105 layers in the radial direction. The mesh is refined in the rotor wake region, where 20 points per aerodynamic wavelength (based on an estimation of the Taylor micro-scale) are used, which is consistent with the third order numerical scheme to ensure reduced dissipation and dispersion errors.

III. Numerical assessment of the WM-LES

WR- and WM-LES are performed on a radial slice of a periodic sector of the ECL5 fan/OGV stage to assess the validity of the WM assumption for the prediction of the aerodynamic and acoustic results.

Figure 5 shows numerical results from WM and WR cases for the isentropic Mach number M_{is} and the root-mean-square (RMS) pressure fluctuations, p_{rms}, on the rotor blade surface. The isentropic Mach number M_{is} is defined

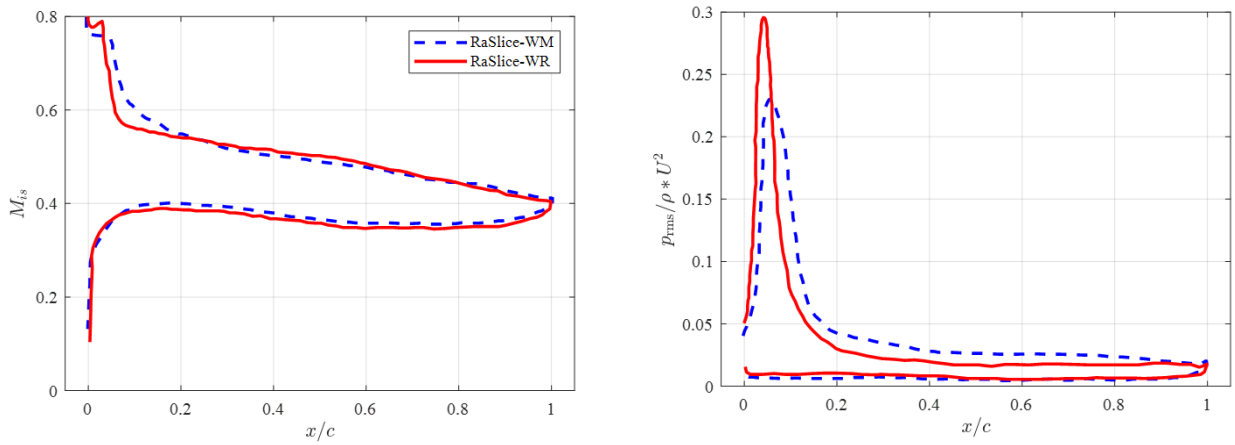

(a) (b)

Fig. 5 Chordwise distribution of (a) the isentropic Mach number M_{is} and (b) RMS pressure fluctuations p_{rms} along the rotor blade at mid-span.

as,

$$M_{is} = \sqrt{\left(\left(\frac{P_0}{p}\right)^{\frac{\gamma_h - 1}{\gamma_h}} - 1\right)\frac{2}{\gamma_h - 1}},$$

where P_0 is the total pressure in the free-stream outside the boundary layers, p is the static pressure and γ_h is the specific heats ratio ($\gamma_h = 1.4$). The distributions of M_{is} and p_{rms} on the pressure side, where the boundary layer remains laminar, are very similar for both WR- and WM-LES. On the suction side, a flow separation zone can be identified by a flat region of isentropic Mach number near the leading edge. It should be noted that high levels of pressure fluctuations are also observed in that region. Some discrepancies between WM and WR results can be found for both M_{is} and p_{rms} in this region. A slightly longer and a lower peak of p_{rms} is predicted by the WM case in comparison with the WR case. These differences remain small and localized in the p_{rms} peak region. Moreover, for the full-span configuration, the separation flow region only concerns the highest radii. Overall, this justifies the use of the WM assumption, for the full-span LES.

IV. Aerodynamic results

In this section, the aerodynamic results for the full-span sector LES are presented. The two broadband noise mechanisms that are studied in this paper, i.e. the rotor-stator interaction noise and the trailing edge noise, are directly related to the turbulent flows in the fan/OGV inter-stage and close to the fan and OGV surfaces. Figure 6 shows an isosurface of the Q-criterion colored by the vorticity magnitude. This provides a qualitative description of the turbulent structures developing in the boundary layers and the wakes. A boundary layer transition can be observed near the leading edge of the blade and vanes along the span. Small turbulent structures can be seen downstream of the transition regions. Such structures are diffracted at the trailing edge of the blade and the vanes and generate trailing edge noise. The turbulent structures in the rotor wake impinge on the leading edge of the stator, which generates rotor-stator interaction noise. On the rotor blade surface, a small recirculation bubble can be found at approximately 60% of the full span, which is characterized by a high vorticity magnitude and leads to the boundary layer transition in this region. It was observed by the authors in a previous study [33] that such a recirculation bubble is generated due to relatively high angles of attack upstream of the rotor blade. Finally, a small corner separation and a tip leakage vortex can be observed where large turbulent structures are found.

Figure 7 presents contours of the averaged streamwise velocity component, u, and the turbulent kinetic energy, k_t, at different spanwise positions. In the rotor domain, the averaging is performed in the rotating reference frame, whereas it is performed in the fixed reference frame in the stator domain. This explains the discontinuity observed at the interface between both domains. For the different spanwise positions, the region of high streamwise velocity component on the suction side of the fan can be associated with the blade loading. Moving from hub to tip, this region is shifted towards the trailing edge and its extent decreases. This is mainly due to the geometry of the fan blade profiles, which are

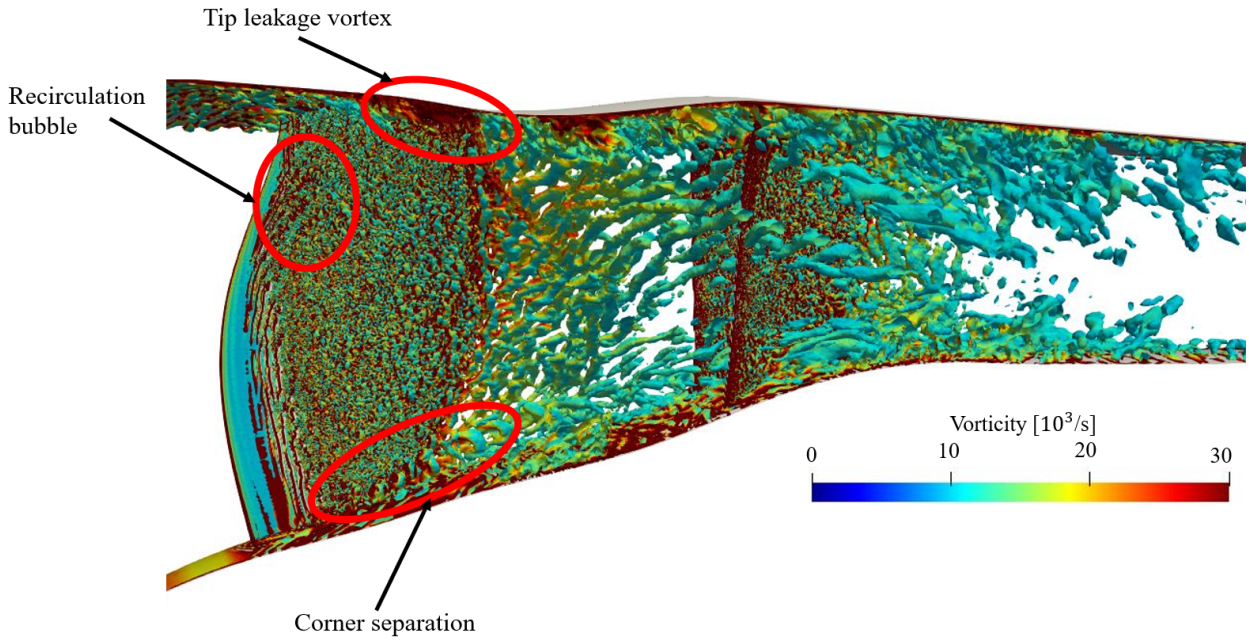

Fig. 6 Iso-surface of Q-criterion ($Qc^2/U^2 = 10$), colored by the vorticity magnitude, for the full-span sector LES.

designed to operate in a transsonic regime at the nominal fan speed (100Nn). Indeed, the camber is reduced from hub to tip, and the maximum camber position is shifted over the suction side of the blade towards the trailing edge. At nominal speed, the flow is transsonic near the fan tip, and the pressure difference is dominated by shock waves. In the present LES, at 55Nn, the flow remains subsonic and the blade loading depends on the angle of attack and the camber.

The transition of the boundary layer to turbulence can be seen from the contours of k_t. For all the spanwise positions, the boundary layer remains laminar over the pressure side of the blade. At 80% of the blade span, a small recirculation bubble can be observed close to the leading edge on the suction side of the rotor blade. This corresponds to a small region of negative streamwise velocity close the blade leading edge in Figure 7 (c) and to the high vorticity magnitudes in Figure 6. The recirculation bubble leads to an earlier transition of the boundary layer to turbulence, compared to the transition at 30% and 50% of the blade span. Additionally, the rotor and stator wake widths seem to remain nearly constant along the span, despite the presence of a small separation region and the increase of the relative speed in the upper half to the span. This may be explained by the decrease of the blade thickness as the radial position increases, which aims at reducing the blade deformation due to centrifugal forces at nominal speed and limit the acceleration at the tip.

At 99% of the span (Figures 7 d and 7 h), the flow topology can be observed in the tip gap region. A complex flow can be seen in this region, which is produced by the formation of a tip leakage vortex (TLV). The TLV can be identified by the low streamwise velocity and is characterized by large levels of turbulent kinetic energy. Unlike previous studies on the tip leakage flow in a fan stage at approach condition [34–36], the TLV appears relatively close to the trailing edge, which may be related to the blade tip geometry and the tip clearance, which is larger than 1% of the chord length and increases towards the trailing edge. Furthermore, the blade airfoil at the tip presents a significant change in the slope between the leading edge and the maximum camber position, the airfoil is relatively flat and thin, and the position of the maximum camber is located at 70% of the chord length.

Figure 8 shows a comparison of the distributions of isentropic Mach number, M_{is}, which is related to the static pressure distribution, from LES and RANS over the rotor blade surface for various spanwise positions. Similar results are obtained at the two radial positions, except in the region close to the leading edge on the suction side at 80% of the rotor span. In this region, a plateau can be seen for the LES, which shows the apparition of the small recirculation bubble, as discussed in Figures 6 and 7. When compared different spanwise positions, a small hump is observed between $x/c = 0.4$ and $x/c = 0.6$ on the suction side of the blade at 80% of the span, which confirms that as the radius increases the blade loading is shifted towards the trailing edge (see Figure 7).

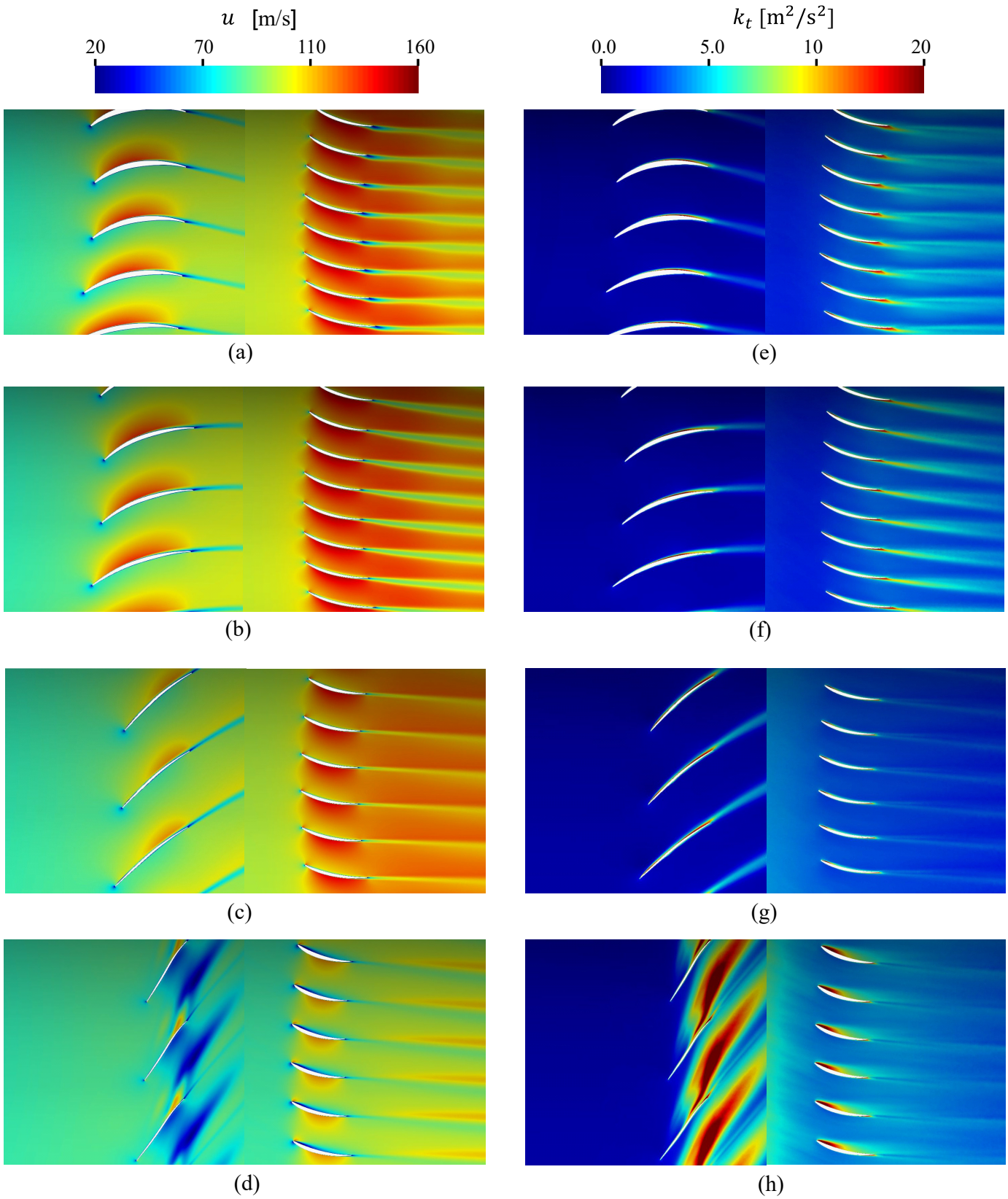

Fig. 7 Contours of the averaged streamwise velocity (left) and the turbulent kinetic energy (right) from WM-LES for various spanwise positions, (a,e) 30%, **(b,f)** 50%, **(c,g)** 80% **and (d,h)** 99%**.**

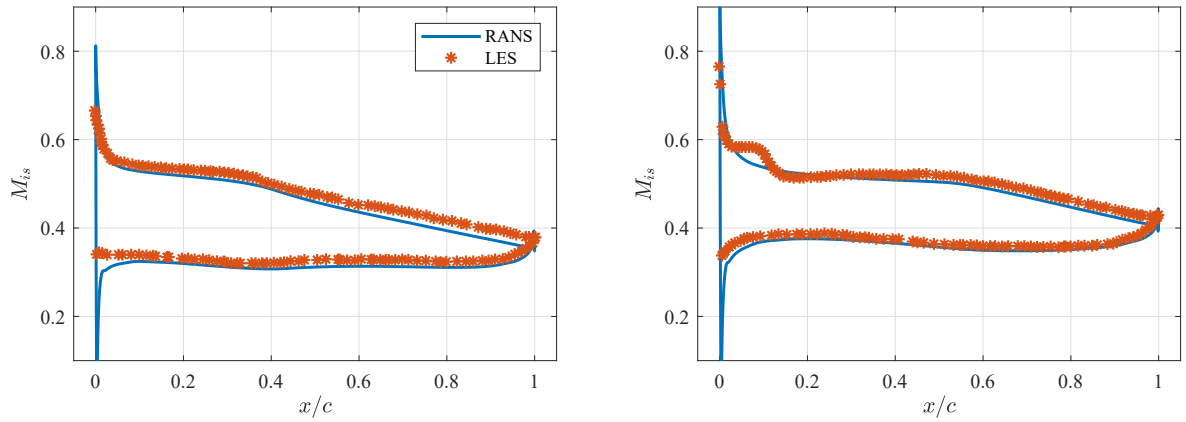

Fig. 8 Comparison between the RANS and LES predictions of the average isentropic Mach number at (a) 50% and (b) 80% of the rotor span.

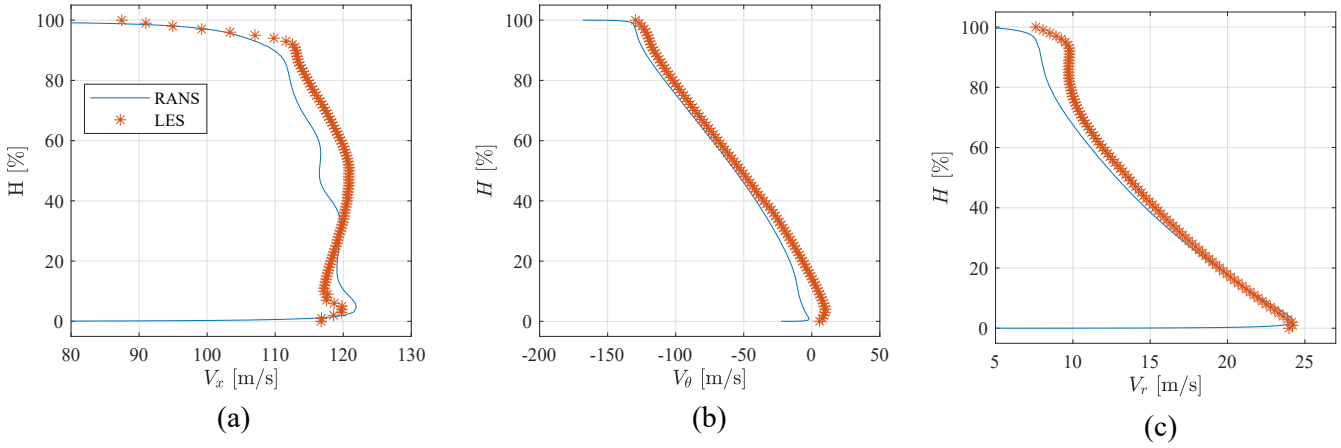

Fig. 9 Comparison between the RANS and LES predictions of the radial profiles of the velocity components in the rotor wake.

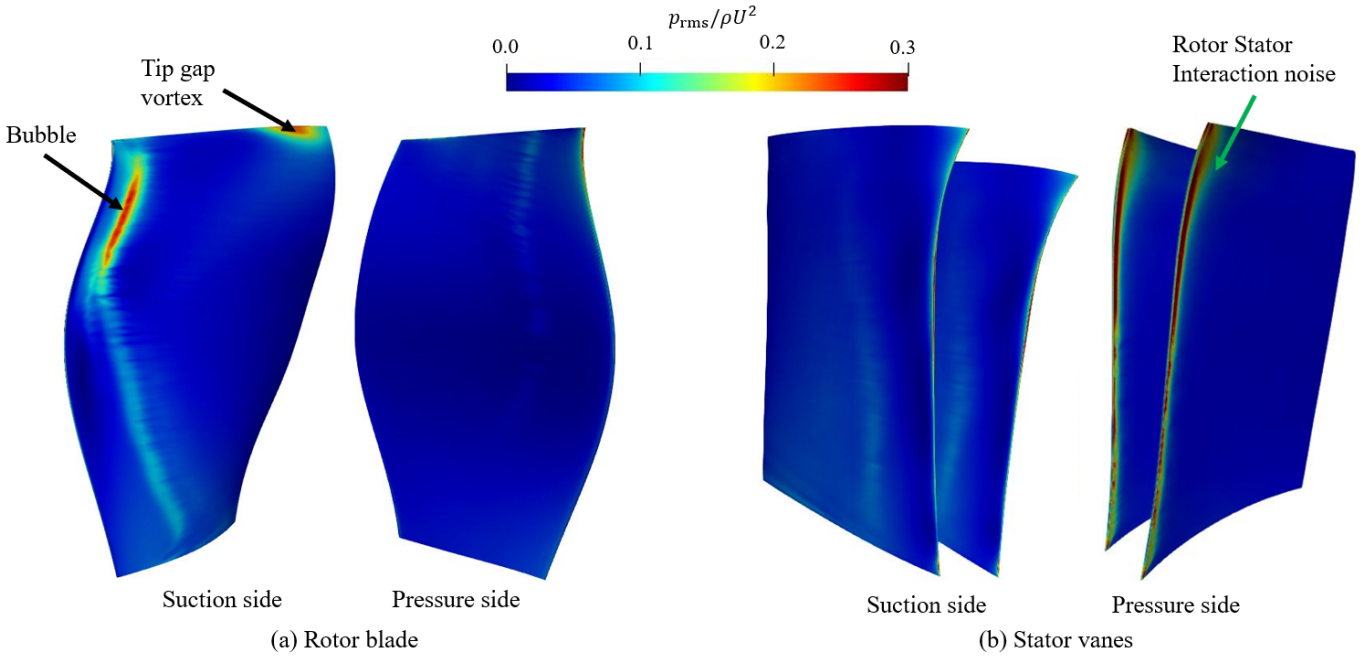

Fig. 10 RMS pressure fluctuations on (a) the fan and (b) OGVs.

The radial distribution of the mean flow velocity components in the rotor wake, V_x, V_θ and V_r, from LES and RANS simulations, is presented in Figure 9. These time-averaged velocity profiles are obtained from the circumferential average of the velocity field at $0.5c$ downstream of the rotor trailing edge. A good agreement can be observed between the LES and RANS results for the three velocity components. In both LES and RANS approaches, a sudden increase in V_x can be seen close to the hub, below 10% of the span, which may correspond to the corner separation in Figure 6. When compared to the LES results, V_x is slightly overpredicted by the RANS below 20% of the rotor span, whereas it is underpredicted above 40% of the span. The TLV region is characterized by a deficit of V_x near the shroud. The radial extent of this region is larger with RANS, which may be explained by the limitations of RANS turbulence modeling in this highly vortical flow. Some differences can also be observed for V_r above 50% of the span, which may be caused by the presence of the recirculation bubble in the LES in this region and the misprediction of the TLV region by the RANS.

V. Aeroacoustic results

A. Noise sources

The location of the noise sources from the fan and OGVs can be estimated from the RMS pressure fluctuations, as shown in Figure 10. High values of p_{rms} are observed in the bubble and the rotor tip regions, which is consistent with the location of intense turbulent structures, as shown in Figure 6. High p_{rms} values can also be found along the leading edge of the OGVs, which is related to the rotor-stator interaction noise. It should be noted that no boundary layer separation is visible on the OGVs. However, the peak in p_{rms} is located on the pressure side of the OGVs, which suggests that the effective angle of attack of the stator is below 0°.

The instantaneous dilatation rate contours, $\nabla.u$, are shown in Figure 11 at 80% of the span. The dilatation rate is useful to identify the flow perturbations that may be considered as noise mechanisms. Hydrodynamic perturbations are shown in the boundary layers and in the wakes. When observing the wave-fronts, two main noise sources can be identified, the trailing edge noise generated at the trailing edges of the rotor blades and stator vanes, and the rotor-stator interaction noise generated at the leading edges of the stator vanes. It should be noted that the quadrupole noise sources from the wakes seem to be negligible when compared to dipole sources at the trailing edges and the leading edges.

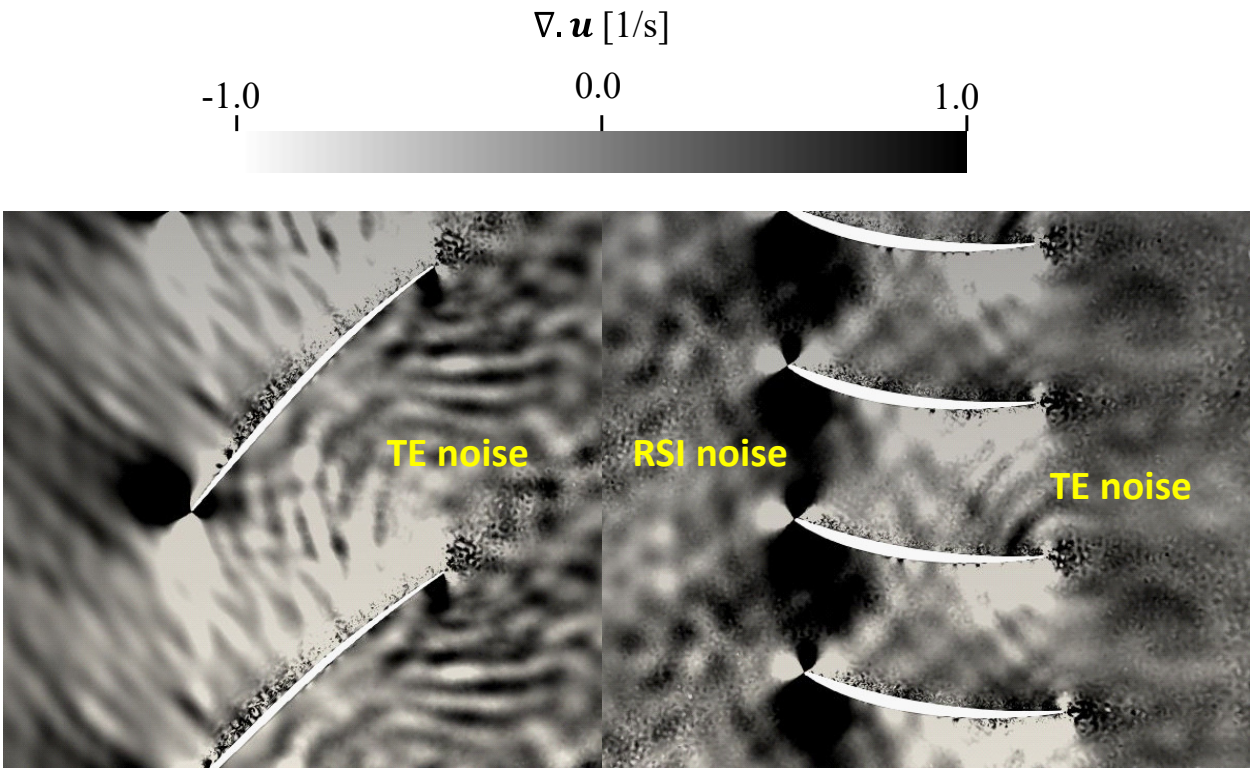

Fig. 11 Instantaneous contours of the dilatation rate in a blade-to-blade view at 80% of the rotor span.

B. Input data for the rotor-stator interaction noise analytical models

The rotor-stator interaction noise is computed using the flow statistics upstream of the stator leading edge extracted from the LES. The input parameters are: (i) the axial velocity and the velocity magnitude, (ii) the turbulent kinetic energy and turbulence integral length scale, and (iii) the wake half-width. These parameters are extracted at a distance of $0.03c$ upstream of the stator leading edge, which is sufficient to avoid a significant turbulence distortion near the stator [37, 38].

The radial distribution of absolute velocity magnitude, V_{abs}, and turbulent kinetic energy, k_t, from LES and RANS simulations are compared in Figure 12. Both parameters show similar trends between LES and RANS simulations, except in the corner separation region, where higher values are obtained from the RANS simulation, and in the recirculation bubble and tip regions, where the RANS simulation predicts lower values. Additionally, when compared to the LES, a slight over-prediction of k_t is observed between 20% and 60% of the span for the RANS simulation, which may be due to the difference in the turbulence intensity injected at the inlet plane between the LES and the RANS simulation (a turbulence intensity of 0.5% is injected in the RANS simulation, whereas no turbulence is prescribed in the LES).

In order to calculate the streamwise turbulence length scale, three different approaches are used in this paper. The first approach, which is adopted for the RANS simulation, was proposed by Pope [39] and gives an estimate of the turbulence length scale, λ_p, based on the turbulent variables k_t and ω_t as follows,

$$\lambda_p = C_{Re}\frac{\sqrt{k_t}}{C_\mu \omega_t}, \tag{1}$$

where $C_{Re} = 0.43$ and $C_\mu = 0.09$.

The second approach is based on the empirical law of Jurdic *et al.* [40] and requires the estimation of the wake width L_w, from the numerical simulation. The turbulence length scale in this case, λ_j, is given as,

$$\lambda_j = 0.21 L_w. \tag{2}$$

The third approach is based on Taylor's frozen turbulence assumption [39, 40], which assumes that the turbulent structures are convected unchanged by the mean flow. Temporal recordings collected on an axial cut upstream of the

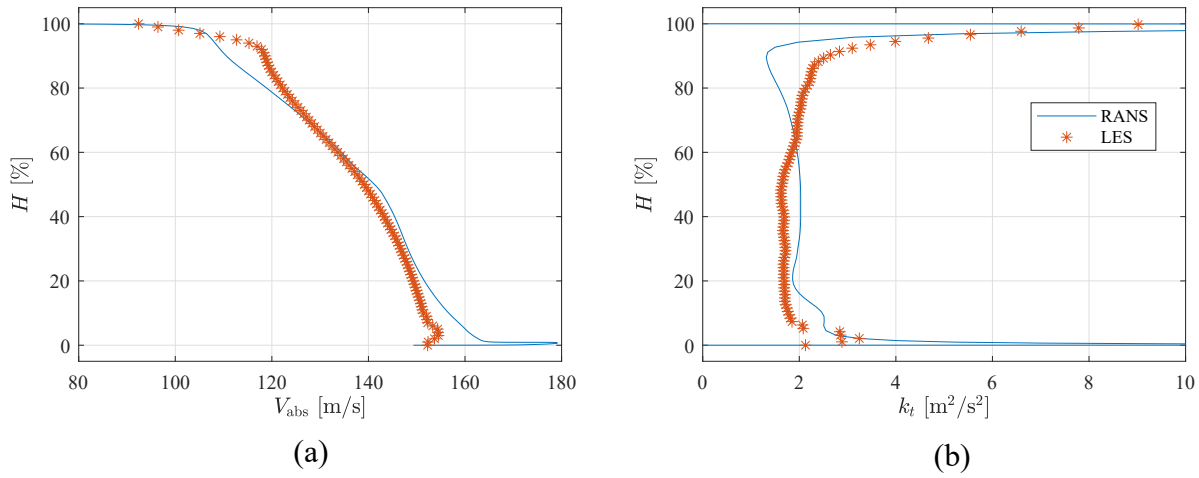

Fig. 12 Comparison of (a) the absolute velocity magnitude V_{abs}, and (b) the turbulent kinetic energy k_t extracted from the RANS and the LES.

stator are used to calculate the autocorrelation function, R_{uu}, from LES as follows,

$$R_{uu}(\mathbf{x},\tau) = \frac{\overline{u'(\mathbf{x},t)u'(\mathbf{x},t+\tau)}}{u_{\text{rms}}(\mathbf{x})^2}, \tag{3}$$

where $u'(\mathbf{x},t)$ is the axial velocity fluctuation at position $\mathbf{x}$ and time t, and $u_{\text{rms}}(\mathbf{x})$ corresponds to the RMS of the axial velocity fluctuation. The time integral scale λ_t can then be computed as,

$$\lambda_t = \int_{\tau=0}^{\infty} R_{uu}(\mathbf{x},\tau)d\tau, \tag{4}$$

and using Taylor's frozen turbulence assumption, the turbulence length scale λ_c can finally be computed as,

$$\lambda_c = \overline{u}\lambda_t, \tag{5}$$

where $\overline{u}$ is the circumferentially-averaged axial velocity component at a distance of $0.03c$ upstream of the stator leading edge.

The radial distributions of the different turbulence length scale estimates, λ_p, λ_j, λ_c, are presented in Figure 13. The levels are consistent between the different approaches but some discrepancies can be observed. Overall, similar trends are obtained for λ_c and λ_j, showing an increase in the length scale above 50% of the span, which can be explained by the recirculation bubble on the fan blade and the tip leakage flow. The absence of the recirculation bubble for the RANS can partially explain the uniform behavior of λ_p from 50% to 90% of the rotor span and the differences with λ_c and λ_j.

In Figure 14, the turbulence velocity spectrum in the streamwise direction, Φ_{uu}, is extracted upstream of the stator leading edge at mid-span from the LES and compared to the model of Liepman as detailed in [41]. λ_c is used as an input for Liepman's model. It should be noted that Φ_{uu} is an input for the analytical models of rotor-stator interaction noise. The tones that appear in the turbulence spectrum from LES correspond to the BPF and its harmonics. From 2 kHz up to the mesh cut-off frequency (20 kHz), a good agreement can be found with the model of Liepman, with slightly higher values for the LES at high frequencies (8-20 kHz). Φ_{uu} is also overpredicted at low frequencies (below 2 kHz) in the LES results, which may be due to the computational domain size in the azimuthal direction and the simulation time.

C. Input data for the trailing edge noise analytical model

The trailing edge noise is computed using the flow properties in the boundary layers close to the trailing edge of the rotor blade and stator vanes. The two parameters for the trailing edge noise analytical model are (i) the wall pressure spectrum, Φ_{pp}, and (ii) the spanwise correlation length, l_z. These parameters can be estimated using empirical laws, for which the input data, such as boundary layer thickness, are extracted from the LES. Figure 15 presents the radial

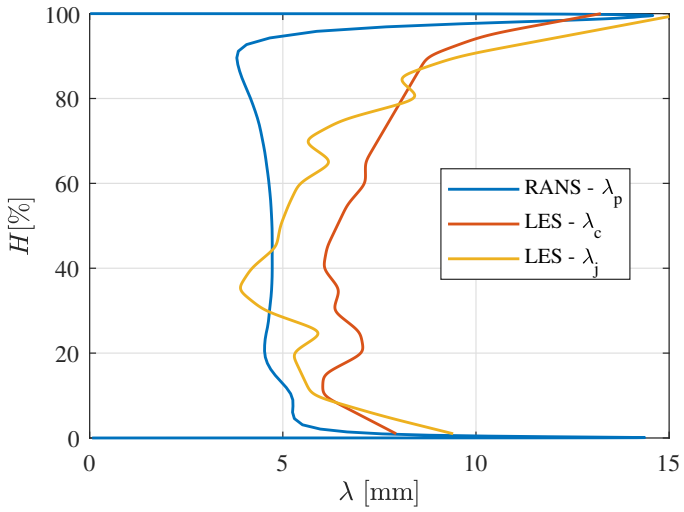

Fig. 13 Comparison of different turbulence length scale estimates extracted from LES and RANS simulation.

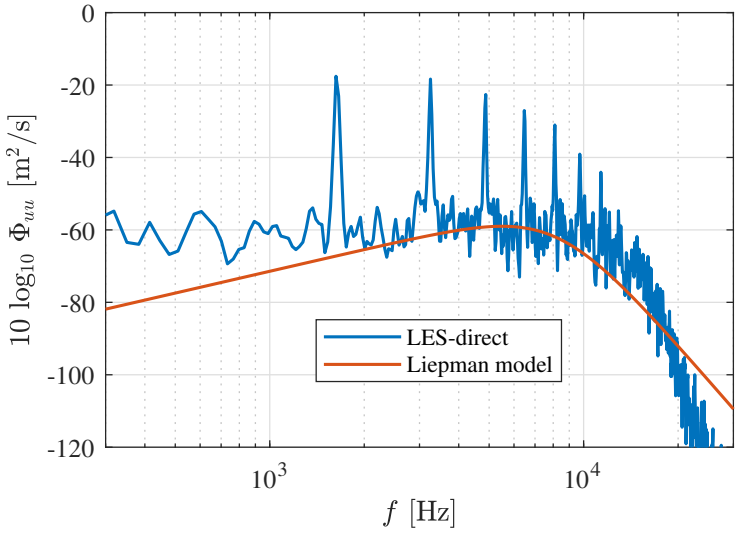

Fig. 14 Comparison of the turbulence velocity spectrum of the streamwise velocity component upstream of the stator leading edge at 50% stator span between the LES and Liepman's model.

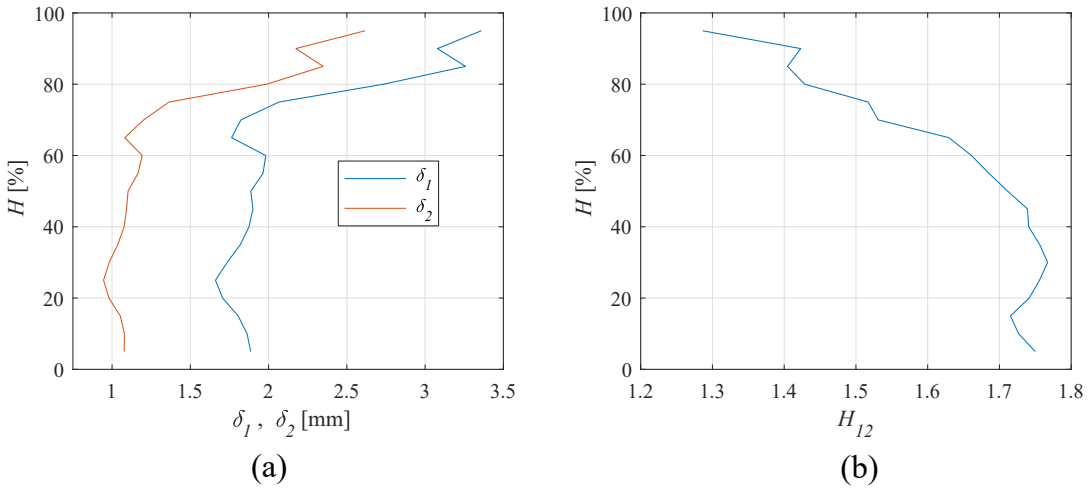

Fig. 15 Radial distributions of the boundary layer parameters on the suction side at $0.02c$ upstream of the rotor trailing edge. (a) Boundary layer displacement and momentum thicknesses δ_1 and δ_2, respectively and (b) and shape factor H_{12}.

distribution of several boundary layer parameters which are extracted on the suction side at $0.02c$ upstream of the rotor trailing edge. The displacement thickness is defined as,

$$\delta_1 = \int_0^{\delta} (1 - \frac{\rho u_b}{\rho_0 U_0}) \mathrm{d}n. \tag{6}$$

The momentum thickness is defined as,

$$\delta_2 = \int_0^{\delta} \frac{\rho u_b}{\rho_0 U_0} (1 - \frac{u_b}{U_0}) \mathrm{d}n, \tag{7}$$

and the shape factor $H_{12} = \delta_1/\delta_2$, where n is the normal wall distance to the suction side surface of the blade, ρ_0 is the free-stream density, U_0 is the velocity magnitude outside the boundary layer, and ρ and u_b are the density and the velocity magnitude within the boundary layer, respectively.

The boundary layer displacement and momentum thicknesses show a similar behavior, and both indicate that there is a significant increase in the boundary layer thicknesses above 70% of the span. In this region, the shape factor presents an important reduction, which varies from 1.67 at 60% of the rotor span to 1.3 close to the tip region. This behavior can be explained by the high levels of turbulence intensity in the boundary layers at rotor spans higher than 60% due to the recirculation bubble and the tip leakage flow.

The wall pressure spectra are fitted with the empirical model of Rozenberg *et al.* [42], which is based on the model of Goody [43] and includes the effects of the Reynolds number and the adverse pressure gradient. Figure 16 (a) shows the comparison of the wall pressure spectrum at mid-span, from the LES (LES-direct) and Rozenberg's model [42]. A similar trend is observed for both predictions, which indicates that the LES results are able to reproduce the behavior of the wall pressure spectrum over the whole frequency range, with a slope of 1.8 at low frequencies ($\omega\delta_1/U_c < 0.5$), -1.1 in the overlap region ($0.6 < \omega\delta_1/U_c < 6$) and -5.2 at high frequencies ($\omega\delta_1/U_c > 8$).

The spanwise correlation length is fitted with the empirical model of Salze *et al.* [44], which is based on the model of Efimtsov *et al.* [45]. In the direct LES approach, l_z is estimated from the coherence function γ of two points at the same axial position and separated by a spanwise distance Δz as follows,

$$l_z(\omega) = \int_0^{+\infty} \sqrt{\gamma^2(\Delta z, \omega)} \cos(k_z \Delta z) d\Delta z, \tag{8}$$

where k_z is the spanwise wavenumber. In order to use Amiet's trailing edge noise model [12, 19], the blade and the vanes are discretized by 20 radial strips. Then, Amiet's model is applied to each strip and the contribution of each strip is summed incoherently. The value of l_z used for each strip is calculated using unsteady data collected from the LES and the integral in Eq.8 is performed over the span of each strip.

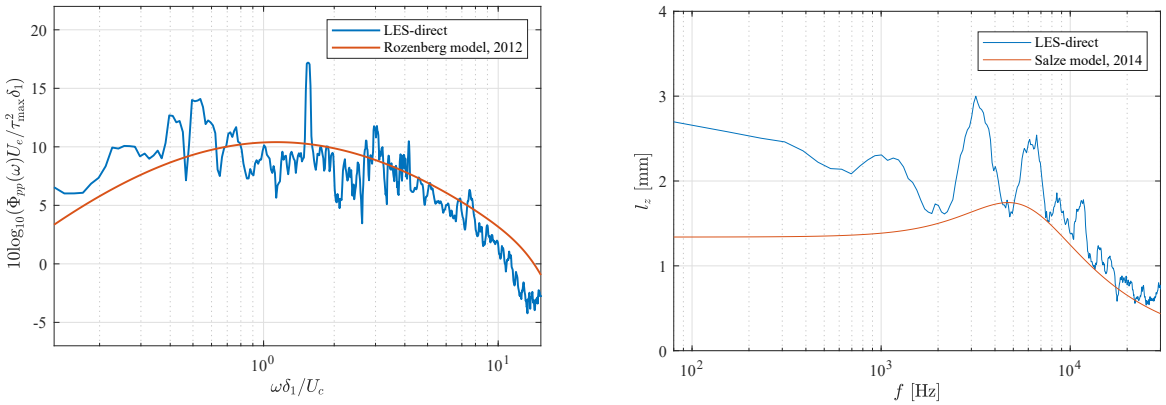

Fig. 16 Input parameters for Amiet's trailing edge noise model at mid-span, from the direct LES approach and empirical models. (a) Wall pressure spectrum. (b) Spanwise correlation length.

Figure 16 (b) presents the comparison of the spanwise correlation length, l_z, at mid-span from the LES (LES-direct) and the model of Salze *et al.* [44]. For the direct LES approach, peaks at approximately 3200 Hz, 6400 Hz and 9600 Hz can be observed. The frequencies of these peaks correspond to the first three harmonics of the vane passing frequency VPF = $V\Omega/60$, where Ω is the fan rotation speed in RPM, and $V = 32$ corresponds to the number of vanes in the full stage. Since the monitor points collect data in the rotating frame, the presence of these tones can be associated with the periodic interaction of the rotor wakes with the stator vanes. Overall, a good agreement is observed between the predictions directly obtained from the LES (LES-direct) and the model of Salze *et al.* [44] at high frequencies ($f > 4$ kHz), whereas an over-prediction of the LES at low to mid frequencies can be observed in the LES. This frequency range corresponds to length scales of the order of the spanwise extent of the computational domain. Periodic boundary conditions are used on the azimuthal boundaries, which imposes a perfect correlation between the azimuthal boundaries and may explain the over-prediction at low to mid frequencies.

D. Noise prediction

The direct noise computation of the sound power levels from the LES is compared to the predictions of the analytical models. For the analytical modeling, the code *Optibrui* is used and the contributions of both the rotor-stator interaction noise, which is analytically predicted by Hanson's [13] and Posson's [14, 15] models, and the trailing edge noise from the rotor blade and stator vanes, which is modeled by Amiet's trailing edge model [12, 19], are added. The rotor blade and stator vanes are discretized by 20 radial strips. For the rotor-stator interaction noise, the input data described in Section V.B are extracted from the LES at a distance of $0.03c$ upstream of the stator leading edge for each strip. For the trailing edge noise, the input data described in Section V.C are extracted at 98 % of the chord length on the suction side of the rotor blade and the stator vanes for each strip. For the direct LES predictions, unsteady probes are located in the duct upstream of the rotor (intake section at two chord lengths upstream of the rotor) and downstream of the stator (exhaust section at two chord lengths downstream of the stator), where the mesh remains sufficiently refined to properly propagate the acoustic waves. The locations of the extraction planes are chosen such that the hub radius remains nearly constant upstream and downstream of the intake and exhaust sections, respectively. A comparison of the sound power levels (SWL) from the two approaches is shown in Figure 17. A fairly good agreement is obtained between the approaches. However, an under-prediction of the sound levels from the analytical models can be observed over the whole frequency range. This may be partially explained by additional noise sources that are present in the LES and are not modeled by the analytical models, such as the tip gap noise (due to the tip leakage vortex shown in Figures 6 and 10). It is known that the tip gap noise can have a contribution at lower frequencies, where the largest discrepancies can be found. When compared both analytical models, noise predictions using the model of Posson *et al.* [14, 15] are lower, especially at low frequencies, which may be due to duct cut-off effects that are included in Posson's model and are neglected in Hanson's model.

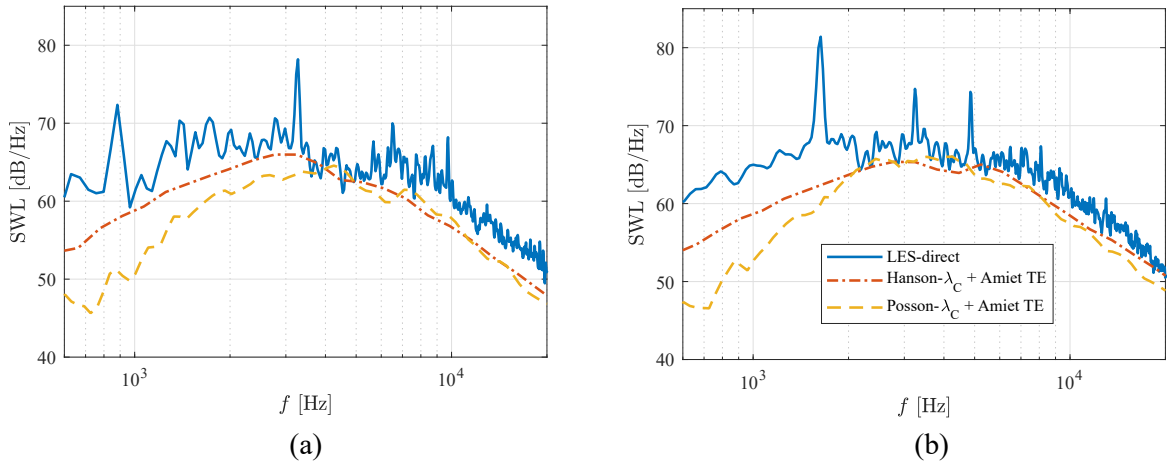

Fig. 17 Sound power levels from the direct LES approach and the analytical models at (a) the intake and (b) the exhaust sections.

VI. Conclusions

In the present study, two broadband noise mechanisms in an UHBR fan/OGV stage are investigated at approach conditions using high-fidelity LES. The mesh is carefully refined to meet both turbulent requirements, especially in the boundary layers and wakes, and acoustic requirements, away from the wall, which allow for a direct computation of the noise from the LES in the near field of the rotor and stator.

Several mean and turbulent flow quantities obtained from the LES are compared to a RANS simulation on the same configuration. The aerodynamic results show a good agreement between both numerical approaches, except in highly turbulent regions close to the tip leakage flow near the blade tip, the corner separation near the blade hub and the recirculation bubble region. The latter extends from 60% to 90% of the rotor span and is only observed in the LES.

Sound power levels deduced directly from the LES are compared with LES-informed analytical models. The input data for the models are obtained from the LES. Two analytical models are used for the rotor-stator interaction noise, including Hanson's [13] and Posson's [14, 15] models. Different approaches are used to estimate the turbulence length scale upstream of the stator leading edge. Similar trends are obtained when using Jurdic's model [40] and the autocorrelation function, which is associated with Taylor's frozen turbulence assumption and based on unsteady recordings from the LES [39, 40]. The turbulence velocity spectrum of the streamwise velocity component is also extracted from the LES and compared to Liepman's model [41], which is informed with LES data. The results from Liepman's model seem to match well the LES results, especially at mid to high frequencies, which justifies its use in Hanson's and Posson's models.

The analytical trailing edge noise model used in this study is based on Amiet's work [12, 19] and describes the scattering of pressure fluctuations from an incident boundary layer at a sharp trailing edge. The main input parameters of this model are the wall pressure spectrum and the spanwise correlation length. Each of these parameters is extracted from the LES at the suction side of the rotor blade and stator vanes close to the trailing edges and is fitted with empirical models from the literature, for which the input data are also taken from the LES. The wall pressure spectrum is fitted with Rozenberg's model [42], which includes the effects of the Reynolds number and the adverse pressure gradient. When the direct LES spectrum is compared to the spectrum predicted by Rozenberg's model at the rotor mid-span, a good match is found with slightly larger values for the model at mid to high frequencies. The spanwise correlation length is fitted with the model of Salze *et al.* [44] and the results from both the LES and Salze's model are compared at the rotor mid-span. A good agreement is obtained at high frequencies. However, higher values of the spanwise correlation length are obtained with the LES when compared to the model at low to mid frequencies, which can be partially explained by the limited azimuthal extent of the computational domain.

Finally, the noise predictions using the rotor-stator interaction noise and the trailing edge noise analytical models underestimate the noise compared to the LES results over the whole range of frequency. This suggests the presence of additional noise sources in the LES, such as the tip leakage noise and the corner separation noise, that are not reproduced by these analytical models.

Acknowledgments

This work was performed within the framework of the industrial chair ARENA (ANR-18-CHIN-0004-01) co-financed by Safran Aircraft Engines and the French National Research Agency (ANR), and is also supported by the Labex CeLyA of the Université de Lyon, operated by the French National Research Agency (ANR-11-LABX-0060/ ANR-16-IDEX-0005).
The computational resources were provided by GENCI (CINES, project number A0102A05039) and by FLMSN-PMCS2I at Ecole Centrale de Lyon.
The authors would like to thank Safran, Airbus and Valeo for providing access to the Optibrui software.
The authors also acknowledge Michel Roger, Stéphane Aubert and Danny Lewis from the Laboratoire de Mécanique des Fluides et d'Acoustique of Ecole Centrale de Lyon and Hélène de Laborderie de Safran Aircraft Engines for their precious advice.
Most of the post-processing was performed using Antares (release 1.16.0, https://www.cerfacs.fr/antares).

References

[1] *Aeronautics and Air Transport: Beyond Vision 2020 (Towards 2050)*, Tech. Rep., ACARE Strategy Review Group, The advisory council for aeronautics eesearch in Europe (ACARE), 2010. URL `https://pq-ue.ani.pt/brochuras/h2020/transportes/a-background-document-from-acare.pdf`.

[2] Envia, E., "Fan noise reduction: an overview," *International Journal of Aeroacoustics*, Vol. 1, No. 1, 2002, pp. 43–64. https://doi.org/10.1260/1475472021502668.

[3] Moreau, S., "Turbomachinery noise predictions: present and future," *Acoustics*, Vol. 1, No. 1, 2019, pp. 92–116. https://doi.org/10.3390/acoustics1010008.

[4] Law, T., and Dowling, A., "Reduction of aeroengine tonal noise using scattering from a multi-segmented liner," *14th AIAA/CEAS Aeroacoustics Conference (29th AIAA Aeroacoustics Conference)*, 2008. https://doi.org/10.2514/6.2008-2978.

[5] Tyler, J., and Sofrin, T., "Axial flow compressor noise studies," *Society of Automotive Engineers Transactions*, Vol. 70, 1962, pp. 309–332. https://doi.org/10.4271/620532.

[6] Peake, N., "Elements of Aviation Acoustics," *The Aeronautical Journal (1968)*, Vol. 98, No. 980, 1994, pp. 405–406. https://doi.org/10.1017/S0001924000027056.

[7] Peake, N., and Parry, A. B., "Modern challenges facing turbomachinery aeroacoustics," *Annual Review of Fluid Mechanics*, Vol. 44, 2012, pp. 227–248. https://doi.org/10.1146/annurev-fluid-120710-101231.

[8] Lewis, D., de Laborderie, J., Sanjosé, M., Moreau, S., Jacob, M. C., and Masson, V., "Parametric study on state-of-the-art analytical models for fan broadband interaction noise predictions," *Journal of Sound and Vibration*, Vol. 514, 2021. https://doi.org/10.1016/j.jsv.2021.116423.

[9] Moreau, S., and Roger, M., "Advanced noise modeling for future propulsion systems," *International Journal of Aeroacoustics*, Vol. 17, No. 6-8, 2018, pp. 576–599. https://doi.org/10.1177/1475472X18789005.

[10] Amiet, R. K., "Acoustic radiation from an airfoil in a turbulent stream," *Journal of Sound and Vibration*, Vol. 41, No. 4, 1975, pp. 407–420. https://doi.org/10.1016/S0022-460X(75)80105-2.

[11] Amiet, R., "Noise due to turbulent flow past a trailing edge," *Journal of Sound and Vibration*, Vol. 47, No. 3, 1976, pp. 387–393. https://doi.org/10.1016/0022-460X(76)90948-2.

[12] Roger, M., and Moreau, S., "Back-scattering correction and further extensions of Amiet's trailing-edge noise model. Part 1: theory," *Journal of Sound and vibration*, Vol. 286, No. 3, 2005, pp. 477–506.

[13] Hanson, D. B., *Theory for broadband noise of rotor and stator cascades with inhomogeneous inflow turbulence including effects of lean and sweep*, National Aeronautics and Space Administration, Glenn Research Center, CR-2001-210762, 2001.

[14] Posson, H., Roger, M., and Moreau, S., "On a uniformly valid analytical rectilinear cascade response function," *Journal of Fluid Mechanics*, Vol. 663, 2010, p. 22–52. https://doi.org/10.1017/S0022112010003368.

[15] Posson, H., Moreau, S., and Roger, M., "On the use of a uniformly valid analytical cascade response function for fan broadband noise predictions," *Journal of Sound and Vibration*, Vol. 329, No. 18, 2010, pp. 3721–3743. https://doi.org/10.1016/j.jsv.2010.03.009.

[16] Glegg, S. A., "The Response of a swept blade row to a three-dimensional gust," *Journal of Sound and Vibration*, Vol. 227, No. 1, 1999, pp. 29–64. https://doi.org/10.1006/jsvi.1999.2327.

[17] Pérez Arroyo, C., Leonard, T., Sanjosé, M., Moreau, S., and Duchaine, F., "Large Eddy Simulation of a scale-model turbofan for fan noise source diagnostic," *Journal of Sound and Vibration*, Vol. 445, 2019, pp. 64–76. https://doi.org/10.1016/j.jsv.2019.01.005.

[18] Masson, V., Posson, H., Sanjose, M., Léonard, T., Moreau, S., and Roger, M., "Fan-OGV interaction broadband noise prediction in a rigid annular duct with swirling and sheared mean flow," *22nd AIAA/CEAS Aeroacoustics Conference*, 2016. https://doi.org/10.2514/6.2016-2944.

[19] Amiet, R. K., "Noise due to turbulent flow past a trailing edge," *Journal of sound and vibration*, Vol. 47, No. 3, 1976, pp. 387–393. https://doi.org/10.1016/0022-460X(76)90948-2.

[20] Brandstetter, C., Pagès, V., Duquesne, P., Ottavy, X., Ferrand, P., Aubert, S., and Blanc, L., "UHBR open-test-case fan ECL5/CATANA part 1: geometry and aerodynamic performance," *14th European Conference on Turbomachinery Fluid dynamics & Thermodynamics*, Gdansk, Poland, 2021.

[21] Pagès, V., Duquesne, P., Ottavy, X., Ferrand, P., Aubert, S., Blanc, L., and Brandstetter, C., "UHBR open-test-case fan ECL5/CATANA part 2: mechanical and aeroelastic stability analysis," *14th European Conference on Turbomachinery Fluid dynamics & Thermodynamics*, Gdansk, Poland, 2021.

[22] Schonfeld, T., and Rudgyard, M., "Steady and unsteady flow simulations using the hybrid flow solver AVBP," *AIAA Journal*, Vol. 37, No. 11, 1999, pp. 1378–1385. https://doi.org/10.2514/2.636.

[23] Rai, M. M., and Madavan, N. K., "Multi-Airfoil Navier–Stokes Simulations of Turbine Rotor–Stator Interaction," *Journal of Turbomachinery*, Vol. 112, No. 3, 1990, pp. 377–384. https://doi.org/10.1115/1.2927670.

[24] Wang, G., Duchaine, F., Papadogiannis, D., Duran, I., Moreau, S., and Gicquel, L. Y., "An overset grid method for large eddy simulation of turbomachinery stages," *Journal of Computational Physics*, Vol. 274, 2014, pp. 333–355. https://doi.org/10.1016/j.jcp.2014.06.006.

[25] Colin, O., and Rudgyard, M., "Development of high-order Taylor-Galerkin schemes for LES," *Journal of Computational Physics*, Vol. 162, No. 2, 2000, pp. 338–371. https://doi.org/10.1006/jcph.2000.6538.

[26] Nicoud, F., Toda, H. B., Cabrit, O., Bose, S., and Lee, J., "Using singular values to build a subgrid-scale model for large eddy simulations," *Physics of fluids*, Vol. 23, No. 8, 2011. https://doi.org/10.1063/1.3623274.

[27] Poinsot, T., and Lele, S., "Boundary conditions for direct simulations of compressible viscous flows," *Journal of Computational Physics*, Vol. 101, No. 1, 1992, pp. 104–129. https://doi.org/10.1016/0021-9991(92)90046-2.

[28] Schmitt, P., Poinsot, T., Schuermans, B., and Geigle, K. P., "Large-eddy simulation and experimental study of heat transfer, nitric oxide emissions and combustion instability in a swirled turbulent high-pressure burner," *Journal of Fluid Mechanics*, Vol. 570, 2007, pp. 17–46. https://doi.org/10.1017/S0022112006003156.

[29] Al-Am, J., Clair, V., Giauque, A., Boudet, J., and Gea-Aguilera, F., "A Parametric Study on the LES Numerical Setup to Investigate Fan/OGV Broadband Noise," *International Journal of Turbomachinery, Propulsion and Power*, Vol. 6, No. 2, 2021. https://doi.org/10.3390/ijtpp6020012.

[30] Jameson, A., "Origins and further development of the Jameson–Schmidt–Turkel scheme," *AIAA Journal*, Vol. 55, No. 5, 2017, pp. 1487–1510. https://doi.org/10.2514/1.J055493.

[31] Menter, F. R., "Two-equation eddy-viscosity turbulence models for engineering applications," *AIAA Journal*, Vol. 32, No. 8, 1994, pp. 1598–1605. https://doi.org/10.2514/3.12149.

[32] Wilcox, D. C., "Reassessment of the scale-determining equation for advanced turbulence models," *AIAA Journal*, Vol. 26, No. 11, 1988, pp. 1299–1310. https://doi.org/10.2514/3.10041.

[33] Al-Am, J., Clair, V., Giauque, A., Boudet, J., and Gea-Aguilera, F., "On the effects of a separation bubble on fan noise," , 2022. URL https://hal.archives-ouvertes.fr/hal-03583335.

[34] You, D., Wang, M., Moin, P., and Mittal, R., "Large-eddy simulation analysis of mechanisms for viscous losses in a turbomachinery tip-clearance flow," *Journal of Fluid Mechanics*, Vol. 586, 2007, pp. 177–204. https://doi.org/10.1017/S0022112007006842.

[35] Kholodov, P., and Moreau, S., "Identification of noise sources in a realistic turbofan rotor using large eddy simulation," *Acoustics*, Vol. 2, No. 3, 2020, pp. 691–706. https://doi.org/10.3390/acoustics2030037.

[36] Lamidel, D., Daviller, G., Roger, M., and Posson, H., "Numerical prediction of the aerodynamics and acoustics of a tip leakage flow using large-eddy simulation," *International Journal of Turbomachinery, Propulsion and Power*, Vol. 6, 2021. https://doi.org/10.3390/ijtpp6030027.

[37] Santana, L. D., Christophe, J., Schram, C., and Desmet, W., "A Rapid Distortion Theory modified turbulence spectra for semi-analytical airfoil noise prediction," *Journal of Sound and Vibration*, Vol. 383, 2016, pp. 349–363. https://doi.org/https://doi.org/10.1016/j.jsv.2016.07.026.

[38] Gea-Aguilera, F., "Aerodynamic and aeroacoustic modelling of engine fan broadband noise," Ph.D. thesis, University of Southampton, 2017.

[39] Pope, S. B., *Turbulent Flows*, Cambridge University Press, 2000. https://doi.org/10.1017/CBO9780511840531.

[40] Jurdic, V., Joseph, P., and Antoni, J., "Investigation of rotor wake turbulence through cyclostationary spectral analysis," *AIAA Journal*, Vol. 47, No. 9, 2009, pp. 2022–2030. https://doi.org/10.2514/1.36728.

[41] Posson, H., Moreau, S., and Roger, M., "Broadband noise prediction of fan outlet guide vane using a cascade response function," *Journal of Sound and Vibration*, Vol. 330, No. 25, 2011, pp. 6153–6183. https://doi.org/10.1016/j.jsv.2011.07.040.

[42] Rozenberg, Y., Robert, G., and Moreau, S., "Wall-pressure spectral model including the adverse pressure gradient effects," *AIAA Journal*, Vol. 50, No. 10, 2012, pp. 2168–2179. https://doi.org/10.2514/1.J051500.

[43] Goody, M., "Empirical spectral model of surface pressure fluctuations," *AIAA Journal*, Vol. 42, No. 9, 2004, pp. 1788–1794. https://doi.org/10.2514/1.9433.

[44] Salze, É., Bailly, C., Marsden, O., Jondeau, E., and Juvé, D., "An experimental characterisation of wall pressure wavevector-frequency spectra in the presence of pressure gradients," *20th AIAA/CEAS Aeroacoustics Conference*, 2014, p. 2909. https://doi.org/10.2514/6.2014-2909.

[45] Efimtsov, B. M., "Characteristics of the field of turbulent wall pressure fluctuations at large Reynolds numbers," *Sov. Phys. Acoust.*, 1982, pp. 28(4), 289–292.